Self-sustained instability, transition, and turbulence induced by a long separation bubble in the footprint of an internal solitary wave. I. Flow topology

Takahiro Sakai 0*

Department of Aerospace and Mechanical Engineering, University of Southern California, Los Angeles, California 90089-1191, USA

Peter J. Diamessis

School of Civil and Environmental Engineering, Cornell University, Ithaca, New York 14853, USA

Gustaaf B. Jacobs

Department of Aerospace Engineering, San Diego State University, San Diego, California 92182, USA



(Received 22 January 2020; accepted 11 June 2020; published 28 October 2020)

The development of a separated bottom boundary layer in the footprint of a large-amplitude internal solitary wave of depression, propagating against an oncoming barotropic current, is examined in detail using high-resolution implicit large eddy simulation. The wave is supported by a continuous two-layer stratification. The Reynolds number based on the water column height is 1.6×10^5 . This numerical simulation is the first to reproduce the self-sustained three-dimensional vortex shedding, resultant transition, and turbulence under an ISW, which have long been hypothesized to occur in field experiments. No artificial noise is inserted into the flow domain. Part I of this study focuses on a structural description of the sequence of flow regimes developing from a wave-induced, long, high-aspect-ratio, laminar separation bubble. Three illuminating topological features are identified. (a) The spatial development of the self-sustained turbulence is composed of three transitional stages: (i) spontaneous excitation of a global instability in the separation bubble that emanates trailing vortices, (ii) vortex breakup and degeneration into turbulent clouds, and (iii) relaxation to a spatially developing turbulent boundary layer. (b) In the separation bubble, there exists a three-dimensional linear global oscillator, which is primarily excited by the two-dimensional absolute instability of the separated shear layer. This global mode possesses a transverse coherent structure. The transverse perturbation subsequently excites an elliptic instability mode inside the shed vortex, resulting in an axial distortion of the vortex core. (c) A shortwave secondary instability is excited in the form of a series of coherent streamwise vortex streaks that wrap around each shed vortex, leading to rapid break up and burst of the vortex.

DOI: 10.1103/PhysRevFluids.5.103801

I. INTRODUCTION

Internal solitary waves (ISWs) are commonly occurring phenomena in the stratified coastal ocean. In the off-shore region, ISWs of vertical mode-one predominantly occur as waves of depression. The wave-induced horizontal current is largest at the wave trough and decreases in

^{*}tsakai@usc.edu

accordance with the reduction of pycnocline displacement away from the trough. This results in a local minimum pressure beneath the wave trough. The bottom boundary layer (BBL) at the trailing side of the wave thus experiences an adverse pressure gradient (APG), where the boundary layer thickens; if the APG is sufficiently large (i.e., large wave amplitude), then the boundary layer can separate. In the immediate aft of the separation point, the flow is reversed, forming a separated shear layer with an inflectional profile, where a local absolute instability is favorably exited. When such a local pocket of absolute instability is large enough, a global instability can be excited, resulting in a spontaneous shedding of a train of vortices.

The above instability mechanism was first proposed by Bogucki et al. [1] in a study of contaminant and turbidity transport by ISWs of elevation at the Los Angeles basin. Soon thereafter, the existence of global instability was verified by means of a two-dimensional (2D) direct numerical simulation (DNS) [2]. Wang and Redekopp [3] assessed the dependence of the global instability on the wave-based Reynolds number and ISW amplitude. Stastna and Lamb [4] demonstrated, by means of a 2D DNS with use of a fully nonlinear ISW model, that the amplitude of the background barotropic current, and the strength of the vorticity in the associated boundary layer, is also an important determining parameter for the occurrence of global instability. Further exploring the sensitivity of global instability to the strength of background current, the same authors later examined the resuspension of neutrally buoyant particles seeded over the bed [5]. All of the aforementioned studies are based on waves of elevation. For a wave of depression, the global instability mechanism is essentially the same as that of a wave of elevation. This was verified by means of a 2D DNS by Diamessis and Redekopp [6] for a weakly nonlinear wave of depression in the absence of the background current. Later, Aghsaee et al. [7] confirmed the global instability by means of high-resolution 2D DNS for a series of fully nonlinear ISWs and also explored the evolution of the vortex shedding during the wave shoaling onto a sloping boundary.

An experimental study was conducted by Carr and Davies [8] with the objective of verifying the presence of a global instability mode. They measured the reverse flow of a separated shear layer in the footprint of a wave of depression (see Ref. [9] for the cases of wave of elevation), but no manifestation of global instability was observed. The stated explanation was that the Reynolds number they considered was not high enough; viscous dissipation hence suppressed the formation of instabilities. Later this claim was verified by Theim *et al.* [10] in their 2D numerical simulations. In a follow-up paper, Carr *et al.* increased the Reynolds number using waves of larger amplitude, which was enabled by placing a rigid lid over the top boundary that was originally free, and detailed measurements of the near-bed velocity field [11]. They observed a highly coherent vortical wake flow shed by the separated BBL under the ISW. In terms of environmental effects in the footprint of an ISW of depression generated in a laboratory tank, Aghsaee and Boegman [12] reported nonnegligible values of transverse velocities within the near-bed vortex wake, visualized the resuspension of noncohesive sediment and proposed predictive criteria for such resuspension.

Vershaeve and Pedersen [13] conducted a parabolic instability analysis for the spatially dependent bottom boundary layer under surface solitary waves. They extended this analysis to the BBL under fully nonlinear ISWs of depression and identified a convective instability in the case of no oncoming current and no separation bubble under the wave. Their analysis does not account for the potential for global instability and does not give any insight on the 3D dynamics of transition to turbulence.

Extensive recent work by Stastna and coworkers [14–16] has examined the transient 3D response of the ISW-induced BBL to either excitations by localized small-scale perturbations in bottom bathymetry or variable bottom slope [17]. Using bottom-fixed coordinate reference frames, these studies have identified secondary transverse instabilities emerging within vortices within the ISW-driven BBL which, in some cases, appear to become turbulent.

The review article by Boegman and Statsna [18] provides an overview of the instability mechanisms associated with ISW-BBL interaction and a review of all relevant studies to this point. To the best of the authors' knowledge, no studies and none of these particular studies tracked the ISW-induced turbulent BBL over a flat bottom in uniform depth water and over long-development

distances and long-evolution times in a wave-following reference frame. As such, the self-sustained nature of turbulence in the wave footprint has not yet been explored.

A crucial and hitherto unanswered question is whether there exists an intrinsic, self-excited oscillator within the BBL that leads to a self-sustained turbulent flow without any externally inserted perturbations. This question constitutes a nontrivial, quite challenging problem from a computational point of view, in terms of both formulation and cost; the broad range of scales within the transitioning and turbulent bottom boundary layer require a nontrivially large number of degrees of freedom for high-fidelity simulation as we found in a preliminary study [19].

The primary objective of the present work is to document the 3D structure of instability, transition, and the turbulence ultimately resulting in the ISW-induced BBL. A critical unique contribution is the simulation of the wave-induced BBL over long development distances and long integration times. As such, to the best of the authors' knowledge, the simulation reported here is the first highly resolved one of self-sustained 3D instability, transition, and turbulence in the BBL under an ISW. Because the computational cost of this type of simulation is very high and requires significant resources on high-performance computing (HPC) infrastructure, we restrict the study to an optimal model flow configuration, involving a highly nonlinear ISW and sufficiently strong oncoming barotropic current, which reliably reproduce the instability and transition into a self-sustained turbulent BBL at a wave-induced Reynolds number typical of the laboratory.

In an effort to reduce the nontrivially high computational cost and exhaustively long wall-clock time of the final target 3D simulation, we configure an ISW-induced separated flow in a domain of reduced vertical extent that can reproduce realistic initial vortex shedding which mimics what is observed in the equivalent full-size 2D domain. As will be emphasized in Sec. III B, even in such a reduced domain, the target 3D simulation has ultimately expended a total 10 million CPU hours on state-of-the-art HPC platforms. As subsequently described in the remainder of Sec. III, the reduced model configuration is numerically simulated by means of a high-accuracy and resolution, implicit large eddy simulation (LES). In Sec. IV, by examining the coherent structures across all stages of BBL development, we elucidate the flow mechanisms of the self-excited and self-sustained bottom turbulent boundary layer. Relying on the data set obtained in this study, our companion paper (Part II) will examine the mean flow properties and turbulence statistics in the contexts of relaxation of the bottom turbulent wake and bottom sediment resuspension potentially induced by the wave.

II. FORMULATION OF NUMERICAL MODEL

A. Configuration of basic flow model

Focusing on the study of the fundamental physics of ISW-induced BBL development, we consider a 3D channel constituting a nonrotating, nondeformable and smooth wave guide of length $L_x = 26H$ in the streamwise x direction, span of $L_y = 0.15H$ in the transverse y direction and constant depth of H in the vertical z direction. The corresponding velocity field components are denoted as u, v, and w, respectively, as depicted in Fig. 1. A fully nonlinear ISW of vertical mode one of depression propagates in the negative x direction (leftward) with a propagation speed c oriented against the oncoming, barotropic, parallel background current U of a permanent form. The frame of reference is fixed to the ISW, with the origin set to the bottom boundary underneath the local extremum of the wave trough stationed at 6H distance from the left (inflow) boundary. The ISW is stably sustained by a two-layer density stratification as defined by

$$\frac{\rho_s(z)}{\rho_0} = 1 - \frac{1}{2} \left(\frac{\Delta \rho}{\rho_0} \right) \tanh\left(\frac{z - z_0}{d} \right),\tag{1}$$

where $z_0 = 13H/15$, d = H/15, and $\Delta \rho/\rho_0 = 40/1020$.

The basic wave field, which is assumed to be held fixed in time, is modelled by a solution of the 2D Euler equation subject to a uniform, oncoming background current U_0 in the absence of vertical

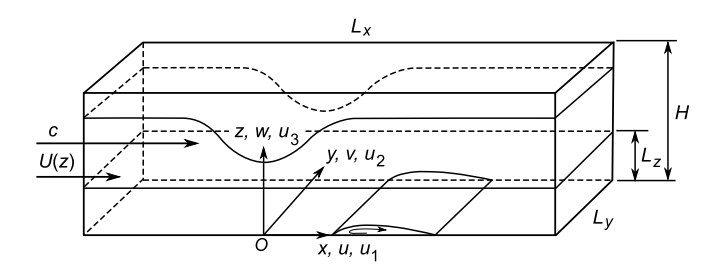


FIG. 1. Schematic diagram of physical model. The frame of reference is fixed to the wave propagating leftward (negative x direction). L_z is a reduced height used for computational domain. In the wave-fixed reference frame, in addition to the background barotropic current, one experiences a uniform current c oriented in the left-to-right x direction. For the sake of visual clarity, in any subsequent figures showing the along-wave velocity, this uniform contribution is omitted.

shear, as described by the Dubreil-Jacotin-Long (DJL) equation,

$$\nabla^2 \eta + \frac{N^2 (z - \eta)}{(c + U_0)^2} = 0, \tag{2}$$

where $\eta(x, z)$ is the isopycnal displacement field; N is the Brunt-Väisälä frequency defined as $N^2 = -g\rho_s'(z)/\rho_0$, where g is the gravitational constant; and c is the Doppler-shifted wave speed. The wave-induced velocity field is defined as

$$\mathbf{u}^{(w)} = (u^{(w)}, 0, w^{(w)}) = (c + U_0)(-\eta_z, 0, \eta_x)$$
(3)

(see Ref. [20]). The DJL equation is solved numerically by employing a freely available computer code (see Ref. [21] for details) that implements Turkington's algorithm [22]. The wave amplitude that we choose for this study is 0.346H, with a wave length λ_w of 2.33H which is defined as $\lambda_w = \int_{-\infty}^{\infty} \eta_p \, dx/\eta_{p\,\text{min}}$, where η_p is the vertical displacement of the pycnocline and $-\eta_{p\,\text{min}}$ is the wave amplitude. Relative to the conjugate state limit [23], the amplitude is of 85% and the wave-induced velocity at the bottom boundary is of 74%, and the wave phase speed is of 99%, representing a large amplitude ISW.

In terms of stability of such a large ISW, the minimum gradient Richardson number Ri = $N^2/(\partial u/\partial z)^2 = 0.26$ (>0.25) is attained in the pycnocline at the wave trough. Consequently, shear (Kelvin-Helmholtz type) instability is not expected along the pycnocline [24–27]. Additionally, the maximum velocity at the upper layer, denoted as u_{wt} , as $u_{wt}/c \approx 0.87$ (<1), is below the breaking limit, suggesting that the wave is well below the convective instability limit [28], a potential driver of subsurface recirculating cores [26,29–31]. The ISW considered here, therefore, can be deemed to sustain its waveform over long propagation distances.

The wave-induced current field is independent of the strength of the background barotropic current, that is, the sum of the Doppler-shifted wave propagation speed (c) and the background current (U_0) is constant. Here we denote $c_{w0} \equiv c + U_0$, which corresponds to the ISW propagation speed in the case of vanishing background current. Moreover, the wave-induced velocity is proportional to c_{w0} , whereby c_{w0} can serve as a reasonable scaling measure for the bottom velocity field. In this study, we set the dimensionless background current, defined as $\hat{U}_0 = U_0/c_{w0}$, to 0.5. The wave-based Reynolds number, defined through c_{w0} , the water depth, and the kinematic viscosity ν ,

$$Re_w = \frac{c_{w0}H}{v} = \frac{(c+U_0)H}{v},$$
 (4)

is 1.6×10^5 . For reference, the Reynolds number defined in terms of the wave-induced velocity in the lower layer, u_{wb} , and the water depth is $\text{Re}_{wb} = u_{wb}H/v = 1.85 \times 10^5$. These Reynolds number

values are comparable, in order of magnitude, to those in laboratory (cf. Refs. [11,12]) and are two to three orders of magnitude smaller than values associated with the oceanic continental shelf.

The wave and background current amplitudes used here, while not uncommon in the ocean [29,32,33], are somewhat large, which is a choice motivated by the limitations of available computational resources. Taking into account the multiscale nature of the problem under consideration and the numerous nontrivial trial simulations, spanning values of $\text{Re}_w = O(10^4 - 10^5)$ and $0 \leqslant \hat{U}_0 \leqslant 0.6$ and a range of medium- to large-amplitude ISWs, carried out prior to the highly costly main production run examined here, our choice of ISW and background current converged toward larger amplitudes for both. As such, the instability of the ISW-induced BBL, subsequent transition and the development of a near-bed turbulent wake, can be reproduced in a domain with dimensions which are optimal, in terms of localizing resolution at the near-bed part of the water column, allowing sufficient downstream BBL development and long integration times and ensuring sufficient resolution of all physically important scales across all stages of BBL evolution.

In order to reduce the computational cost down to a more affordable level, the upper 70% depth of the domain is truncated. Such a choice is particularly driven by the fact that our target flow is the bottom-focused ISW-induced BBL, in a two-layer continuous stratification with a characteristically large-scale separation between the ISW and the motions within the BBL. Consequently, the 3D numerical simulation is performed for the lower, unstratified domain, i.e., $L_x \times L_y \times L_z = 26H \times 0.15H \times 0.3H$. A preliminary numerical experiment using 2D DNS simulations (not shown) has shown that the reduced domain is able to produce a similar flow, in terms of the structure and frequency of the global instability, compared to that obtained with the full-depth (stratified) domain. The 3D effects, including higher-order instability and turbulence, can eventually drive the resulting turbulent wake to reach locally to the vicinity of top boundary of the reduced domain; yet such local irregularities are suppressed by means of a sponge layer (see a related discussion in Sec. IV A).

As will be shown in Sec. IV, the domain width $L_y = 0.15H$, which is kept to minimal due to computational resource constraints, is sufficiently large to reproduce a self-sustained turbulent wake. However, the 3D instability mechanism of the resulting separation bubble beneath the wave tail is primarily driven by the 2D global oscillator, which may be a result of choice of such a narrow spanwise domain size. A larger domain width, e.g., comparable to the wavelength or bubble length, is expected to excite a centrifugal global oscillator [34], which can be excited by a much smaller reverse flow ratio in the separation bubble (7% of free stream velocity, see Ref. [34]) compared to our case (over 20% of free stream velocity, not shown). Such a conjecture suggests a possibility that BBL instability and transition may occur for smaller wave amplitude and weaker background current than what is considered here. Moreover, the resulting flow topology change driven by the centrifugal instability can excite a secondary instability [35], leading to a different transition regime that possibly influences the relaxation distance to the developing turbulent boundary layer. Characterization of such 3D global modes and associated flow topology and its bifurcation for ISW-induced separation bubbles under different environmental conditions is the subject of future work.

B. Mathematical model

In terms of mathematical formulation, we follow the same approach as that presented in the earlier work of Diamessis and Redekopp [6]. Several points that are specific to the present study are noted in this section.

The governing equation in the unstratified computational domain involves conservation laws of incompressible flow, with the frame of reference fixed to the wave propagating negative *x* direction:

$$\nabla \cdot \mathbf{u} = 0, \tag{5a}$$

$$\frac{\partial \mathbf{u}}{\partial t} + (\mathbf{u} \cdot \nabla)\mathbf{u} = -\frac{1}{\rho_0} \nabla p + \nu \nabla^2 \mathbf{u} - \mathbf{g} + \mathbf{F}^{(u)}, \tag{5b}$$

where $\mathbf{g} = g\hat{\mathbf{k}}$, where $(\hat{\mathbf{i}}, \hat{\mathbf{j}}, \hat{\mathbf{k}})$ are the standard unit vectors and p is the pressure. $\mathbf{F}^{(u)}$ appearing in the momentum equation is the forcing term that is primarily intended to enforce the wave base flow to sustain a permanent form (see Ref. [6]).

We express the dependent variables in terms of the perturbation to the wave base flow, i.e.,

$$\mathbf{u} = c\hat{\mathbf{i}} + \mathbf{u}^{(B)} + \tilde{\mathbf{u}},
p = p^{(B)} + \tilde{p},$$
(6)

where the variables with tilde are perturbation variables. The variables $(\mathbf{u}^{(B)}, p^{(B)})$ represent the wave base flow, as defined by

$$\mathbf{u}^{(B)} = U(z)\hat{\mathbf{i}} + \mathbf{u}^{(w)}, p^{(B)} = p_s(z) + p^{(w)},$$
(7)

where U(z) is a reference background current for which we allow some vertical variation from U_0 to account for a no-slip shear adjacent to the bed; p_s is the hydrostatic pressure. The wave-induced field $(\mathbf{u}^{(w)}, p^{(w)})$ and the associated eigenvalue c are of a solution set of the DJL equation with the uniform background current U_0 .

The field equation (5) can now be written in terms of the perturbation variables as follows:

$$\nabla \cdot \tilde{\mathbf{u}} = 0, \tag{8a}$$

$$\frac{\partial \tilde{\mathbf{u}}}{\partial t} + [(\tilde{\mathbf{u}} + \mathbf{c}) \cdot \nabla] \tilde{\mathbf{u}} = -\frac{1}{\rho_0} \nabla \tilde{p} + \nu \nabla^2 \tilde{\mathbf{u}} - \{(\mathbf{u}^{(B)} \cdot \nabla) \tilde{\mathbf{u}} + (\tilde{\mathbf{u}} \cdot \nabla) \mathbf{u}^{(B)}\}, \tag{8b}$$

where $\mathbf{c} = c\hat{\mathbf{i}}$ is the wave propagation velocity. The forcing terms do not explicitly appear in the equation after cancellation of terms.

For the background current U(z), while it is arbitrary in nature, we particularly choose a Blasius profile not only because it is a well-defined laminar flow solution but also because it has been well studied in terms of instability and laminar-to-turbulent transition, which can provide useful diagnostic tools in assuring a quiescent inflow state. The thickness of the Blasius boundary layer is set to 0.05H. For the Blasius boundary layer, applying the Michel's method [36], an empirical correlation to locate a laminar-to-turbulent transition point, we find that the critical Reynolds number based on the momentum thickness is 940. In our case, the corresponding Reynolds number at the inflow is 500 (see Part II), which is well below the threshold of laminar-to-turbulent transition. An examination of the effect of the Blasius boundary layer thickness on wave-induced BBL instability is outside of the scope of the present study.

It is possible to directly solve the DJL equation with a nonuniform background current U(z) to obtain the wave-induced field (e.g., see Ref. [20]). However, since the near-bed shear of U(z) is essentially a viscous contribution, it is physically inconsistent to incorporate such a viscously generated bottom shear in the DJL equation which is purely dictated by inviscid dynamics. To this end, the DJL equation is solved with a uniform background current (U_0) and the resulting interaction between the near-bed shear and the inviscid (DJL) wave-induced field is eliminated by the forcing terms

In contrast to laboratory experiments, full-scale flows in typical coastal ocean environments are turbulent [37]. One may be tempted to introduce turbulence in the background flow upstream of the ISW, at least in the BBL. To this end, any additional modification that can cause bypass transition, such as artificial forcing and superposition of disturbance noise to the flow field, is not performed. This conscious choice is made to demonstrate the development of intrinsic and spontaneous BBL-induced global instability and subsequent transition to self-sustained turbulence. The dynamical response of the global instability and subsequent development of turbulent BBL, subject to distrubed or turbulent background current with arbitrary mean velocity profile, is deferred to future work.

At the bottom boundary, an impermeable, no-viscous-slip condition is applied (i.e., $\mathbf{u} = \mathbf{c}$ at z = 0). The perturbation velocity field thus develops through the mismatch of the DJL-generated

ISW horizontal current field with the no-slip condition at the bed. At the upper boundary ($z = L_z$), a stress-free, impermeable boundary condition is imposed, and a sponge layer with a thickness of 10% of the computational domain height ($L_z = 0.3H$) is inserted in order to suppress flow reflection at the boundary. The computational domain is chosen to be periodic in both streamwise (x) and spanwise (x) directions, with a sponge layer of thickness x being inserted at the both streamwise boundaries of the domain, which ensures a laminar, unperturbed incoming flow.

III. NUMERICAL METHOD SPECIFICS

A. Numerical method

A high-accuracy and-resolution parallelized flow solver [38], based on a spectral multidomain spectral penalty method in the vertical, Fourier discretization on the horizontal plane and stiffly stable, and high-order variable time stepping, is employed for the time integration of the field equations. Along with dealiasing of the nonlinear terms, additional stabilization is enabled through application of an exponential spectral filter to suppress spurious energy build-up at the smallest resolved scales and to ensure stable long-time integration. The filter function used for the spectral filter is defined as $\sigma = \exp[-\alpha(m/M)^q]$, where $\alpha = -\ln \epsilon_M$ with ϵ_M being the machine precision, m is the mode index, and M is the maximum mode index. The order of the filter is chosen to be $q_F = 12$ in both streamwise and spanwise directions and $q_L = 14$ in vertical directions over the lower-half portion of the computational domain with a smooth transition to $q_F = q_L = 8$ in all three spatial directions over the upper half of the domain. The horizontal filter is applied once at every time step, and the vertical filter is applied after each fractional step of the operator splitting scheme (advection, pressure, and viscous step) for every time step.

B. Grid resolution

The numerical resolution is chosen to be $N_x \times N_y \times N_z = 12\,288 \times 128 \times 480$ (approximately 750 million points). Twelve spectral subdomains are used in the vertical with 40 points per subdomain. The time-step value ranges from $0.00011\delta_s/c_{w0}$ to $0.0013\delta_s/c_{w0}$, resulting in a total of approximately 1.1 million time steps. The model configuration is simulated from the undisturbed state for $0 < t < 9.0\lambda_w/c$ (where $c = 0.5c_{w0}$). The initial spin-up up to time $t = 6.1\lambda_w/c$ is used for saturation of the domain with a developed wake flow. The time thereafter is allotted for statistical data collection. This remaining time has a duration of $t = 2.9\lambda_w/c$ which corresponds to a total of 80 vortex shedding cycles.

The resulting total computational time has accumulated to approximately 10 million CPU hours. This number includes time associated with model setup, preliminary, and production runs. There are several factors that necessitate such a long computer time. First, an unusually long domain is required because the BBL develops several wavelengths downstream. In parallel, one needs to ensure that the spanwise domain is wide enough to resolve a near-gravest transverse instability mode. The nonperiodic vertical domain requires a very small near-wall mesh sufficient to resolve the near-wall physics. Vigorous vortex shedding and subsequent ejection of a faster fluid across the BBL ultimately reduce the early-time time-step value by an order of magnitude. Compared to the domain length, the spanwise domain dimension is two orders of magnitude smaller. The resulting significantly smaller value of N_y , with respect to N_x , constrains the maximum number of MPI processes to N_y . Finally, the number of OpenMP threads has been restricted to no more than two per MPI process because threading has been found to be inefficient on 1024 or more cores for the present model configuration and flow solver.

In Table I, the grid resolution is compared to that used in published numerical investigations of aerodynamic separated flows. N in the table represents the number of grid points within nine wall units in the vertical direction. In the calculation of the viscous wall unit in Table I, the maximum value of time- and-spanwise-averaged bottom friction coefficient c_f (see Part II) has been used [i.e., $\Delta x_i^+ \equiv \Delta x_i/l_{\tau}$, where $l_{\tau} \equiv v/(u_{\infty} - c)\sqrt{c_{f\text{max}}/2}$]. Taking into account that the high-order spectral

TABLE I. Comparison of grid resolution of current study in viscous wall units with that of previous aerodynamic investigations

Case	Δx^+	Δy^+	Δz^+	$N _{z^{+} < 9}$	$Re_{\theta s}^{b}$	Re_{xs}^{b}	Class
Spalart and Strelets [39]	20	6.7	1.0	10	_	10 ⁵	DNS
Alam and Sandham [40]	20.7	6.2	0.9	16	246	_	DNS
Cadieux et al. [41]	26.4	27.5	1.0	_	_	10^{5}	LES, near-wall-resolution
Present study	8.2	4.6	0.027	27	1260	4×10^{5} c	Implicit LES, high-resolution

^aMomentum thickness Reynolds number at the flow separation point.

filters identified above leave undamped the lower 50% of Fourier and Legendre modes, the present study is still comparable with a DNS, particularly in terms of the near-wall region which is actually far more better resolved than what is achieved in published DNS. There are 18 vertical grid points within the viscous sublayer ($z^+ < 5$) and 123 points in the viscous wall region ($z^+ < 50$). Such a high resolution clearly obviates the need for any wall modelling.

IV. RESULTS AND DISCUSSIONS

A. Spatial flow development

Figure 2 shows a typical picture of the instantaneous spanwise perturbation vorticity ω_y taken at the midspan over the entire region of the BBL wake. The vorticity is scaled by using the characteristic velocity c_{w0} and the boundary layer thickness at the point of separation (i.e., a point at which the mean skin friction vanishes), measured as $\delta_s = 0.136H$. Laminar vortices are spontaneously and continually shed from the separated shear layer with a period of $0.169H/c_{w0}$, which is slightly shorter than that measured in 2D simulations (0.174 H/c_{w0}). The shed vortices are first ejected upward and advected downstream, interacting with the bottom boundary, generating vortices of opposite sign along the way, where the majority of the vortices are paired and merge into larger vortices (see at x = 3.5H in the same figure). Some vortices pair and merge on more than one occasion as they advance downstream, depending on their vorticity strength and distance relative to neighboring vortices. The grown vortices then quickly break up into chaotic 3D motions and transition to turbulence in the form of a localized cluster of small-scale motions, referred to as a turbulent "cloud" hereafter. The turbulent cloud further undergoes a rapid expansion in both the streamwise and vertical directions. Further downstream the turbulent clouds become weaker by smearing out (diffusion) at the interface between turbulent and nonturbulent regions and by the associated dissipation of turbulent kinetic energy; the topmost portion of such weakened clouds slightly reach into the top sponge layer.

The development of such a thick turbulent wake is surprising because, for the corresponding 2D simulation (not shown), the vertical extent of the resulting vortex train is much smaller (less than a half) than that of the turbulent cloud, which was another reason for us to decide the height of the reduced computational domain. While the sponge layer at the top boundary damps out the local turbulence entering into the layer and prevents reflections, the presence of the artificial rigid upper wall can modify the mean flow, as inferred by a weak forward pressure gradient along the developing turbulent boundary layer (see Part II). Nevertheless, as will be described in Part II, such a weak pressure gradient is negligibly small compared to the wave-induced pressure gradient in the wave footprint.

To facilitate further discussion, the flow domain is characterized roughly into the three regimes: (i) global instability and transition: 2.5 < x/H < 6 ($1.1 < x/\lambda_w < 2.6$); (ii) vortex breakup and formation of turbulent clouds: 6 < x/H < 13 ($2.6 < x/\lambda_w < 5.6$); and (iii) developing turbulent boundary layer: x/H > 13 ($x/\lambda_w > 5.6$).

 $^{{}^{}b}Re_{xs} \equiv U_0x_s/v$, where x_s is the streamwise distance between the flow inlet and the upper wall suction.

^cCalculated using x_s as the distance from the flow inlet to the wave trough.

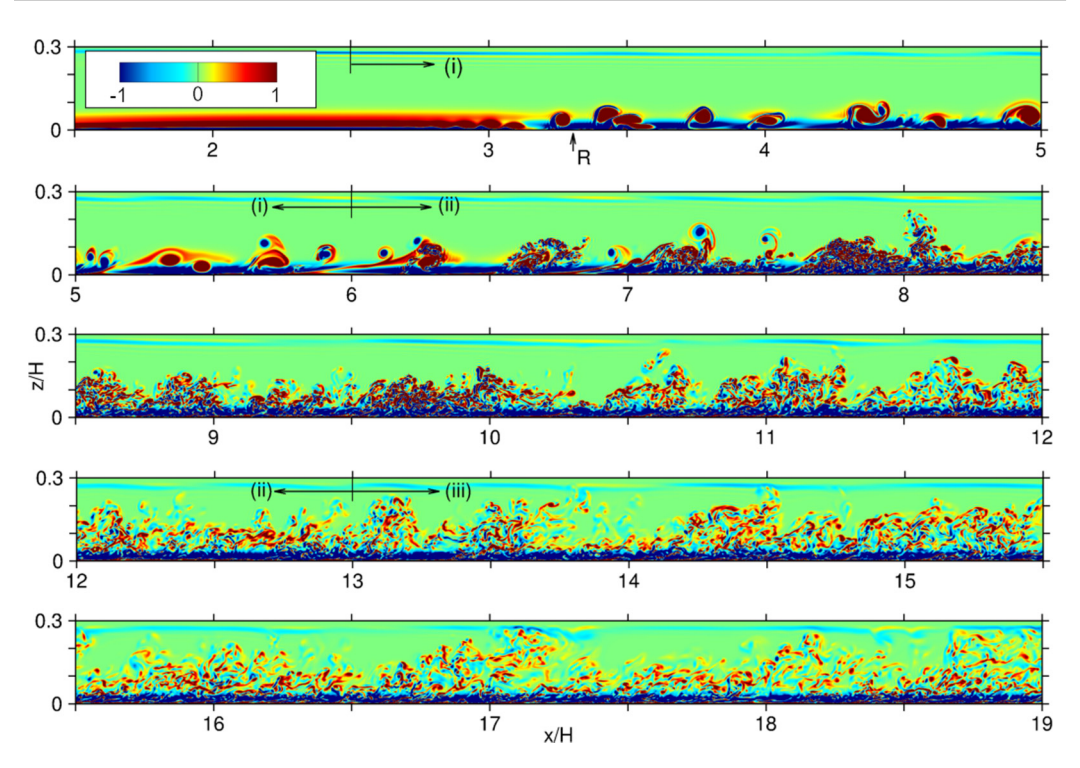


FIG. 2. Spatial development of instantaneous spanwise perturbation vorticity $\omega_y \delta_s/c_{w0}$ over 1.5 < x/H < 19 split equally. Each window has a length of $1.5\lambda_w$. The flow domain is characterized roughly into the three regimes: (i) two- and three-dimensional instability and transition: 2.5 < x/H < 6 ($1.1 < x/\lambda_w < 2.6$); (ii) vortex breakup and formation of turbulent clouds: 6 < x/H < 13 ($2.6 < x/\lambda_w < 5.6$); (iii) developing turbulent boundary layer: x/H > 13 ($x/\lambda_w > 5.6$). The symbol x/t together with an arrow in the top panel indicate the mean reattachment point.

A 3D view of the instantaneous spanwise vorticity, taken at the same time as in Fig. 2, over the transition stage is shown in Fig. 3. The shed vortices appear to be initially two dimensional. They roll over the bottom surface as they translate downstream, where they grow through pairing and merging. The grown vortices then deform, initially bending. The associated isovorticity surfaces strain and ripple axially and circumferentially, in a three-dimensionally complex fashion, leading to ultimately a vigorous breakup into a turbulent cloud. Figure 3 also suggests that the 2D simulation is relevant only for two ISW wavelengths (or in this case about 5H) downstream from the wave trough. Thereafter, three-dimensionality dominates the flow. It is noted that even the two-dimensional stage of the BBL development cannot be simulated by a 2D code because of different downstream feedback.

As per the discussion of Sec. II B, we reiterate that the wave-induced BBL is not seeded with any external disturbances aimed to both initialize vortex shedding and drive its subsequent downstream three-dimensional development and that the inflow Blasius boundary layer state is well below the critical point of laminar-to-turbulent transition. The wave-induced forward pressure gradient ahead of the wave trough accelerates the boundary layer, enhancing stabilization. Moreover, the high-order discretization methods used in all three spatial directions are subject to no or minimal numerical dispersion, a likely source of numerical "noise" that could indirectly play an equivalent instability-generating role; if any such weak very fine-scale disturbances of numerical origin are present in the separating BBL, then they are most likely damped out by the spectral filters. Hence, we are confident that the turbulent wake generated by the ISW-induced BBL is spontaneously generated and self-sustained.

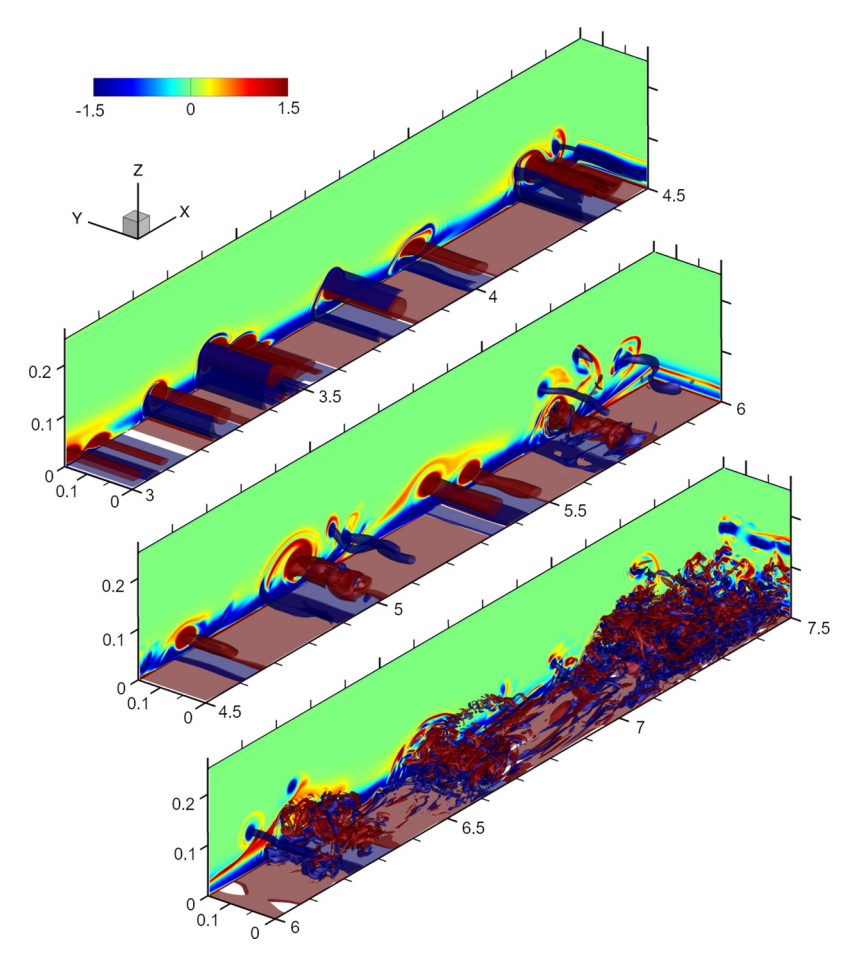


FIG. 3. Spatial development of instantaneous spanwise perturbation vorticity $\omega_y \delta_s/c_{w0}$ in the transition region over 3 < x/H < 7.5 equally split. Each window has a length of $0.64\lambda_w$. Isosurfaces of $\omega_y \delta_s/c_{w0} = 3.0$ (in red) and $\omega_y \delta_s/c_{w0} = -3.0$ (in blue) are shown with a contoured background. All coordinates are scaled by H. Vortex pairing can be seen at $x/H \approx 3.5$. Vortex bending through elliptic instability can be seen at $x/H \approx 5$ and $x/H \approx 5.75$.

It should be added that, at the inflow, the Blasius boundary layer is unstable to external disturbances with frequencies ranging from $0.34c_{w0}/\delta_s$ to $1.07c_{w0}/\delta_s$ [42], where δ_s is the boundary layer thickness at the separation point. These intrinsic (Tollmien-Schlichting wave) modes of the Blasius boundary layer are far from the characteristic frequency of the global instability, measured at $5.07c_{w0}/\delta_s$ (see Sec. IV D), suggesting that their mutual dynamical interaction with the global mode, such as the triggering instability by one mode exciting another mode, is not feasible. Thereby, we reemphasize that the global instability is a dominant dynamical response in the flow regime (i) which drives the self-sustained instability.

B. Presence of three-dimensional global mode

Self-sustenance of turbulence of a spatially developing flow requires an intrinsic, three-dimensionally synchronous eigenstructure beyond the parallel-flow-based counterpart (e.g., see Theofilis [43]). This section provides evidence for the existence of a 3D global mode in the flow under consideration.

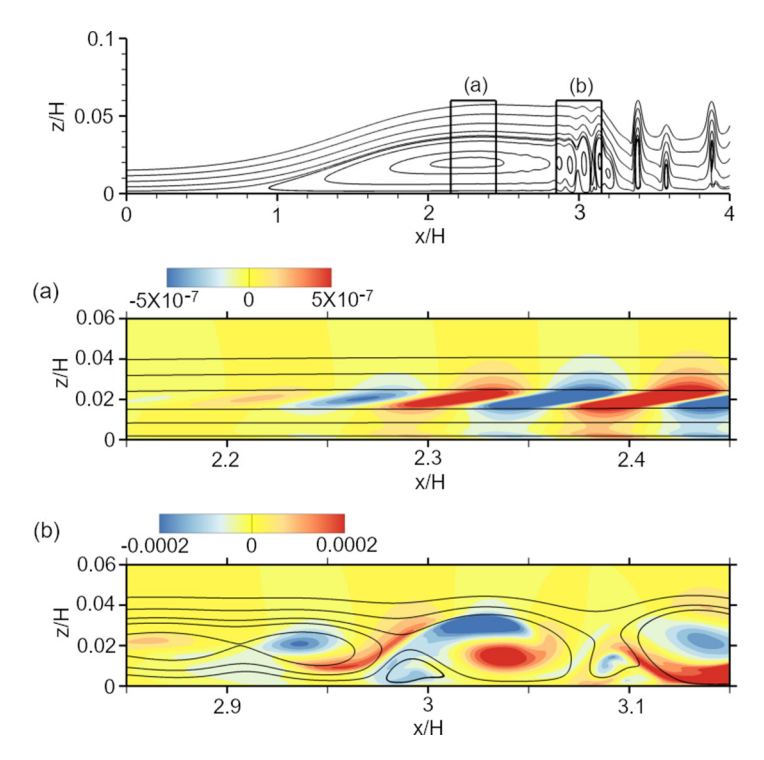


FIG. 4. Contours of instantaneous transverse v velocity scaled by c_{w0} sampled with several instantaneous streamlines at two different downstream locations on the midspan plane: (a) near the maximum reverse flow region. The lower half streamlines flow upstream (to the left) and upper half ones flow downstream; (b) near the aft end of the separation bubble. Boxes in the top panel delineate the location of panels (a) and (b) within the separation bubble.

Figure 4 shows the three-dimensional structure of the instantaneous, transverse v-velocity field taken at the midspan section near the strongest reverse flow region and near the trailing end of the separation bubble, with several instantaneous streamlines superimposed. It is clear from the figure that inclined lobes of alternating sign of the transverse velocity perturbation are oriented along the shear layer of the separation bubble (centered at z/H=0.02; the lower half portion of the streamlines correspond to reverse flow) where the streamlines are nearly parallel. Thereafter, each pair of alternating sign transverse v-velocity perturbations develops into a spanwise vortex core with a spatial growth ratio (defined as $\partial \ln |v|/\partial x$) of roughly $10/H \approx 1.35/\delta_s$; the perturbation pair remains in the vortex core as it advances downstream. This axial disturbance in the vortex core excites an elliptic instability mode, as will be discussed later in this section.

The transverse v-velocity disturbance is associated with distinct streamwise vorticity ω_x , as shown in Fig. 5; the v-velocity contour reveals an inclined vorticity layer, similar in structure, though of opposite sign to the shear layer at the center of the separation bubble, at the immediate vicinity of the bottom boundary. In the same figure, horizontal slices of the vorticity field taken at the shear layer and the bottom boundary are also shown. An alternating, coherent spatial structure is clearly observed both at the shear layer and the bottom boundary in the form of antisymmetric pairs.

The fastest transverse mode reported above has a wavelength equal to the spanwise domain length. However, prior examination of different spanwise domain size (L_y up to 0.4H, not shown) indicated that the fastest-growing mode has a wavelength roughly twice the present domain width.

This observed coherent, three-dimensional eigenstructure extends over the greater length of the separation bubble, which is merely a manifestation of a self-excited global mode. The present

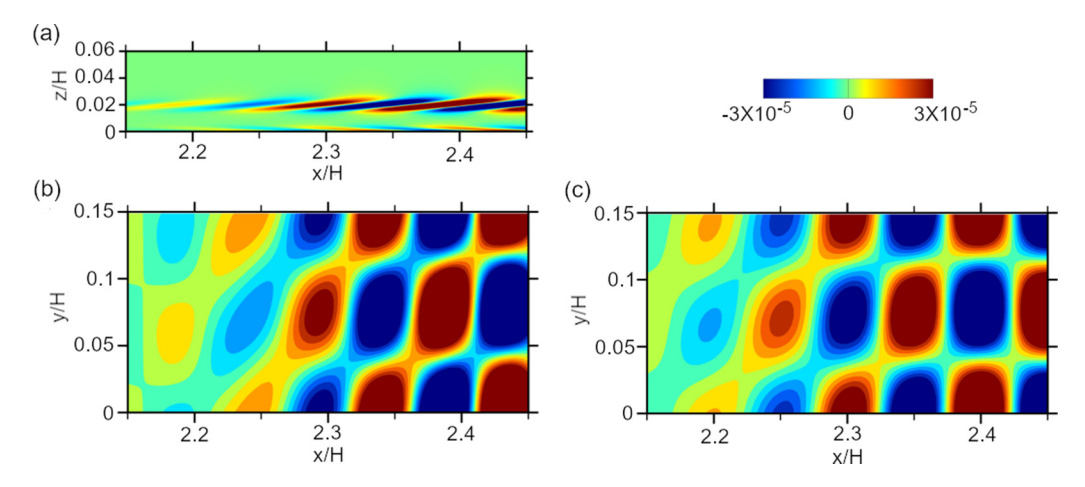


FIG. 5. Contours of instantaneous streamwise vorticity $\omega_x \delta_s / c_{w0}$ near the maximum reverse flow region: (a) cross section at the midspan plane (this section corresponds to the region (a) in Fig. 4), (b) horizontal slice along the primary vorticity layer (z = 0.02H), and (c) horizontal slice along the bottom boundary.

stationary global mode is structurally different from one that was found by Rodríguez and Theofilis [44] in their 3D global analysis of a laminar separation bubble which is about an order of magnitude shorter in length (in term of the bubble aspect ratio) than that of the present case, where the bubble aspect ratio is approximately 85. Their gravest global mode occupies the entire region of the separation bubble, having a cellular structure, with the streamwise length scale coincident with that of the bubble and the transverse length scale about twice the streamwise bubble length. In the present case the streamwise wavelength of the eigenmode is, again, shorter by one order of magnitude, about 1/30 relative to the streamwise bubble length.

According to Rodríguez *et al.* [34], there exist two classes of bubble-induced linear global instability mechanisms. The first class pertains to a linear global oscillator driven by a local pocket of absolute inflectional instability of two-dimensional base flow. The second class pertains to the oscillator driven by a centrifugal instability that has a purely 3D cell structure spanning over the bubble recirculation region. The global oscillator structure of the present flow thus falls into the first class.

Each wave of spatially developing spanwise eigenmode synchronizes with a trailing billow-like vortex that is ejected from the separated shear layer together with one single wave of the spanwise eigenmode inside of the vortex. The shed vortex rolls over the bottom boundary along its way downstream, in a high-strain field exerted by the bottom boundary and neighboring vortices, through which the circumferential streamline is deformed into an elliptical shape. The axial disturbance in the vortex core immediately excites the leading mode of elliptic instability [45]. The spatial structure of the axial perturbation [see Fig. 4(b)] resembles the analytical solution of the gravest elliptic eigenmode for a strained vortex tube in the unbounded domain found by Waleffe [46] (cf. Fig. 2 in Ref. [46]). This axial perturbation bends the vortex core (e.g., see Ref. [47] for similar effects in a corotating vortex pair and Ref. [48] a counterrotating vortex pair), which is manifested as vortex bending revealed in the middle panel (e.g., around x/H = 5 and 5.75) in Fig. 3.

C. Subsequent evolution of three-dimensional instability

To further monitor the downstream evolution structure of a global instability mode discussed in the previous section, Fig. 6 tracks the streamwise vorticity for one arbitrary shed vortex. Isosurfaces of a representative pair of positive and negative streamwise vorticity at several different time instants are shown. In each panel, different contour levels have to be used because of exponential growth of

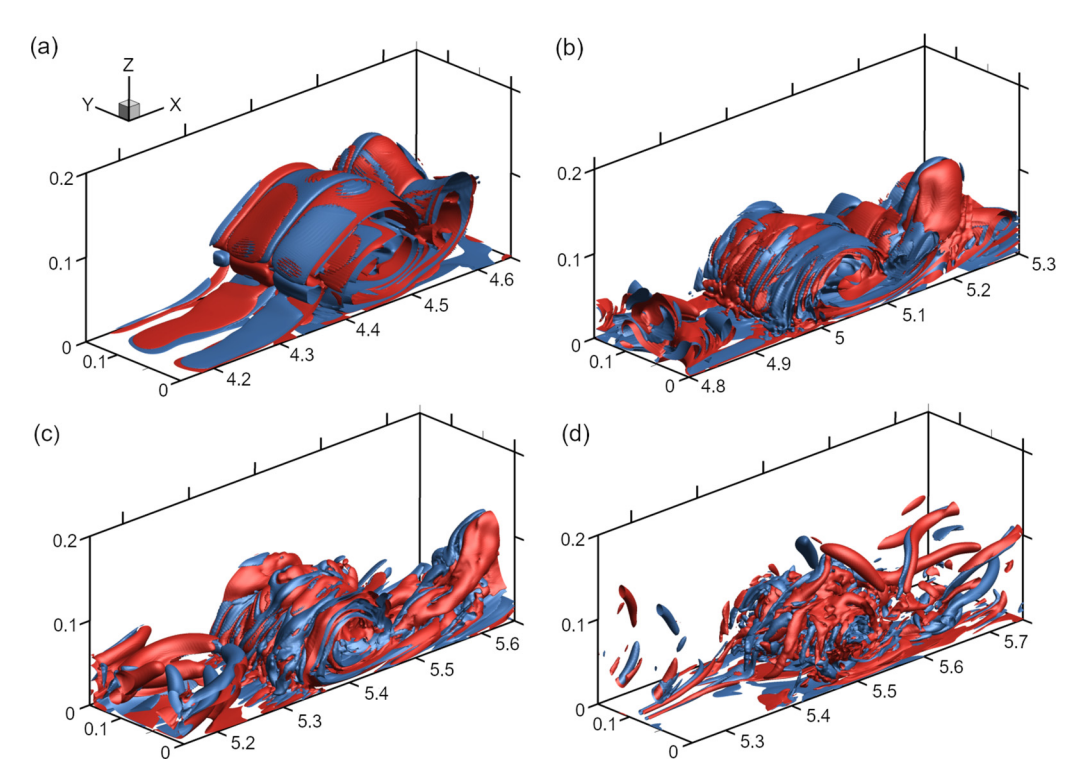


FIG. 6. Isosurface of instantaneous streamwise vorticity $\omega_x \delta_s/c_0$ tracking the same vortex (a) $t=t_0$ with $\omega_x \delta_s/c_{w0}=-0.03$ (blue) and $\omega_x \delta_s/c_{w0}=0.03$ (red), (b) $t=t_0+9.9\delta_s/c_{w0}$ with $\omega_x \delta_s/c_0=-0.06$ (blue) and $\omega_x \delta_s/c_{w0}=0.06$ (red), (c) $t=t_0+13.2\delta_s/c_{w0}$ with $\omega_x \delta_s/c_{w0}=-0.5$ (blue) and $\omega_x \delta_s/c_{w0}=0.5$ (red), and (d) $t=t_0+17.1\delta_s/c_{w0}$ with $\omega_x \delta_s/c_{w0}=-2.0$ (blue) and $\omega_x \delta_s/c_{w0}=2.0$ (red). All coordinates are scaled by H.

the instability. In the figure, a pair of laminar vortices is already merged into one single vortex. It can also be observed that the initially flat streamwise vortex sheet [see Fig. 4(a)] becomes stretched circumferentially and it is rolled around the vortex core [Fig. 6(a)]. The associated vorticity sheet at the bottom boundary is also stretched and wraps around the vortex. After this stage, a short-wave instability is observed in the form of a row of streaks oriented along the outer shell of the vortex [Fig. 6(b)]. The streaks rapidly grow almost entirely and simultaneously from interior to exterior of the vortex [Figs. 6(c) and 6(d)]. The transverse wavelength of the short-wave instability is roughly $0.06\delta_s$, which corresponds approximately 30 viscous-wall lengths.

It is well known that visualizations of vorticity in chaotic or turbulent flows may not reveal as clearly as desired any coherent vortices within such flow fields. On one hand, the choice of the appropriate threshold is not necessarily objective. On the other hand, visualization of vorticity magnitude cannot separate vortex sheets from coherent vortices. Although both such flow structures support strong rotation, the former involve strong strain fields which are negligible in the case of the latter [49]. To circumvent these issues and enable a clearer perspective on coherent structures resulting from the instabilities under consideration, the same vortex is visualized in term of the λ_2 criterion (see Jeong and Hussain [50] for more details) in Fig. 7. This criterion identifies a vortex tube by capturing the local minimum pressure along the vortex axis. In terms of the vortex tracked in Fig. 6, the sheet of streamwise vorticity that appears at the early stage of the spanwise disturbance evolution is not identified as a vortex tube; but the short-wave streaks are identified as vortex filaments in finer scale (compared to the streamwise vorticity counterpart) that appear mostly around the exterior surface of the parent vortex core; the vortex core is quickly filled by

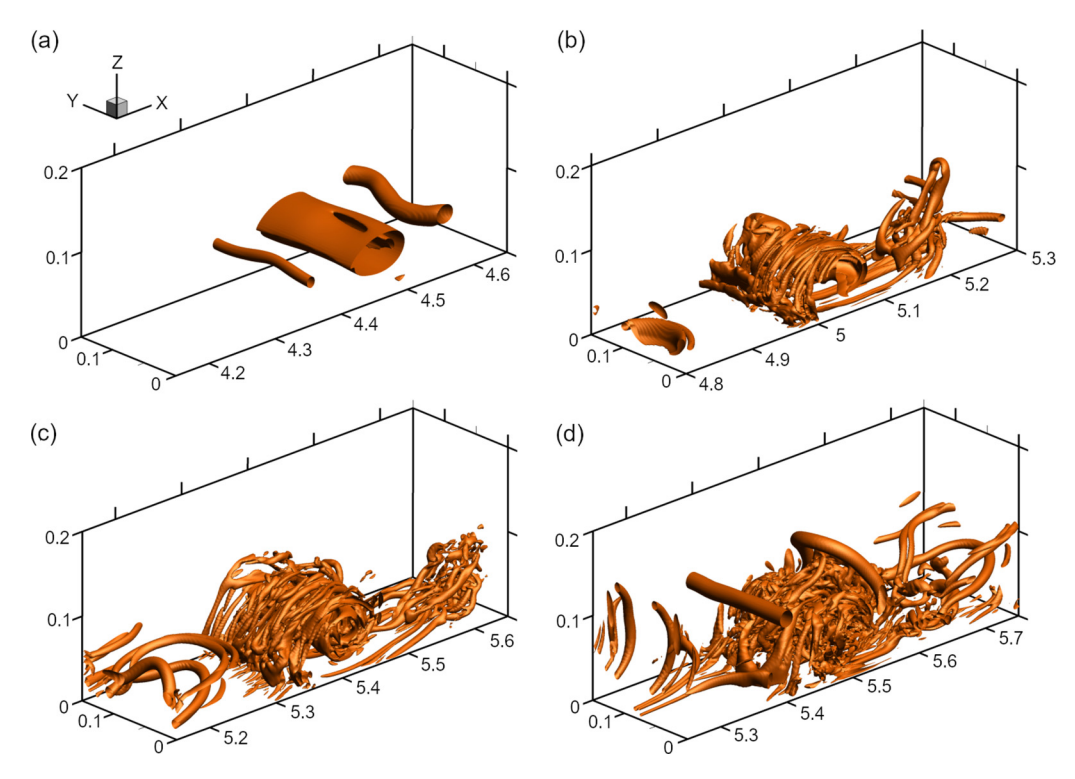


FIG. 7. λ_2 representation of Fig. 6. Isosurface of $\lambda_2 = -0.5$ in all cases: (a) $t = t_0$, (b) $t = t_0 + 9.9\delta_s/c_{w0}$, (c) $t = t_0 + 13.2\delta_s/c_{w0}$, and (d) $t = t_0 + 17.1\delta_s/c_{w0}$. All coordinates are scaled by H.

smaller vortex filaments, presumably through highly nonlinear instability. This cluster of coherent motions associated with the vortex is energetic, as it proceeds with a rapid expansion (increase in size) observed in the bottom panel of Figs. 3 and 8 described below.

In Fig. 8, the spatial evolution of the turbulent clouds is visualized through the λ_2 criterion by coloring the contours of the vertical velocity in the range $|w/c_{w0}| < 0.05$ onto the λ_2 isosurfaces. For 7.5 < x/H < 9 ($3.2 < x/\lambda_w < 3.9$), each cloud is relatively distinct. Within each cloud, there is a clear separation of an upwelling (positive w) and downwelling (negative w) region, which implies that the clouds are still in the process of spatial expansion and that the kinetic energy of the parent vortex has not yet fully cascaded to smaller turbulent eddies. For 10.8 < x/H < 12.3 ($4.6 < x/\lambda_w < 5.3$), the division into upwelling or downwelling regions may still hold, though it is far less clear. For 15.8 < x/H < 17.3 ($6.8 < x/\lambda_w < 7.4$), the turbulent coherent structure over the upper portion of the domain becomes less distinct due to dissipation and diffusion. A virtually uniform turbulent boundary layer is formed over the bottom boundary. Upwelling and downwelling motions have become less intense as compared to the turbulent events upstream.

D. Energy spectra

For the purpose of exploring the development of relevant physical timescales in the turbulent wake evolution, single-point time series of the velocity field are recorded at selected streamwise locations in the wave-fixed reference frame. Figure 9(a) shows typical time series of the wall-normal velocity w sampled at depth $z = 0.2H(=0.183\delta_s)$, at the streamwise stations $x = 3H(\approx 1.3\lambda_w)$, $x = 9H(\approx 3.9\lambda_w)$, and $x = 17H(\approx 7.3\lambda_w)$, all at the midspan (y = 0.075H). The particular streamwise sampling locations are chosen as representative of the different flow regimes shown in Fig. 2.

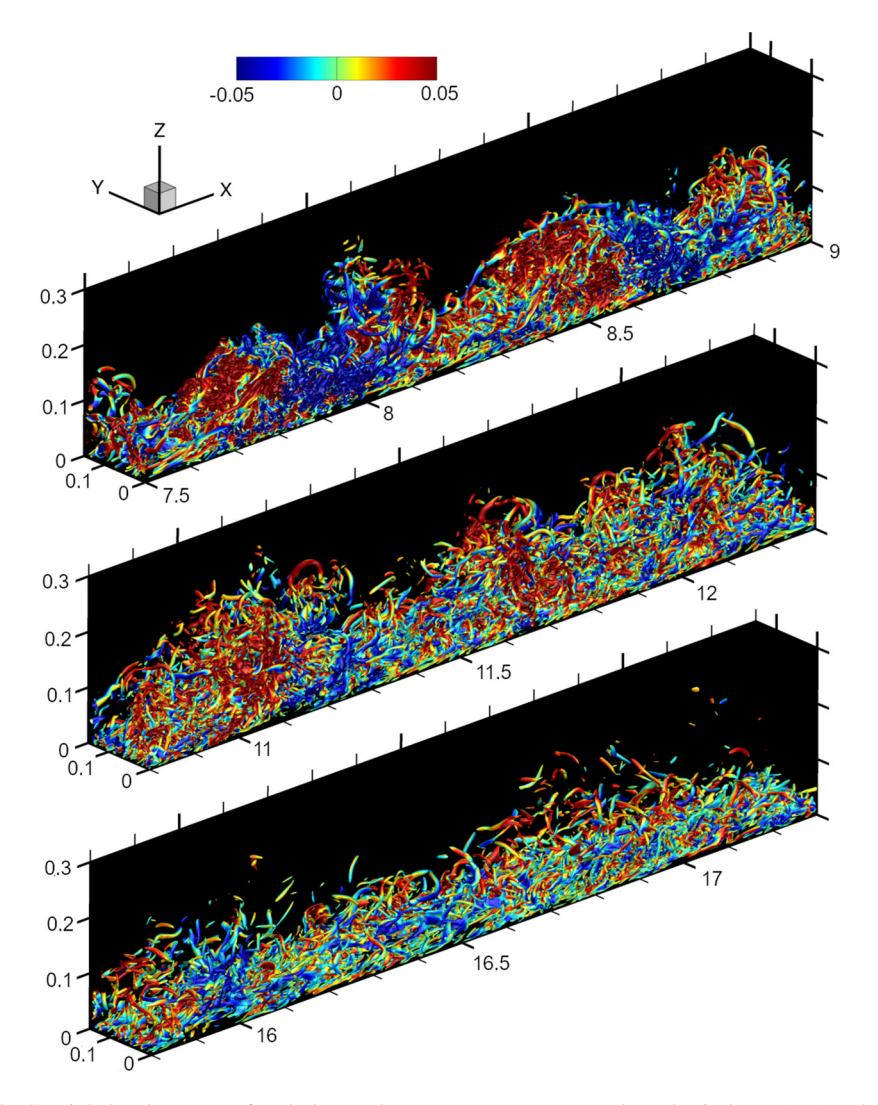


FIG. 8. Spatial development of turbulent coherent structures over selected windows (top) 7.5 < x/H < 9, (middle) 10.8 < x/H < 12.3, and (bottom) 15.8 < x/H < 17.3 (each window has a length of $0.64\lambda_w$). Isosurface of $\lambda_2 = -0.5$ on which the contour of w/c_{w0} is rendered. All coordinates are scaled by H. Pairs of positive and negative w velocities indicate distinct "memory" of vortices shed from the separated shear layer in the upstream (top and middle). Such distinct memory of parent vortices is blurred further downstream (bottom).

Large upwelling velocities are clearly observed, with largest instantaneous values of $w \approx 0.2c_{w0}$ at x = 3H (near the trailing edge of the separation bubble), $w \approx 0.3c_{w0}$ at x = 9H (expansion stage of the turbulent cloud), and $w \approx 0.05c_{w0}$ at x = 17H (developing turbulent boundary layer stage). For reference, the largest vertical velocity of the wave-induced vertical current is approximately $w^{(w)} = 0.3c_{w0}$ which is comparable to the wall-normal velocity values observed in the BBL over the downstream interval extending from the vortex ejection point to the turbulent burst region. At x = 3H, the signal exhibits temporal coherence with modulation of amplitude, but the signal at x = 9H exhibits a longer-period oscillation with large amplitude in the background with short-period random fluctuation superimposed on it. At the developing turbulent boundary layer stage (x = 17H), the signal has a random fluctuation structure typical of turbulent flows.

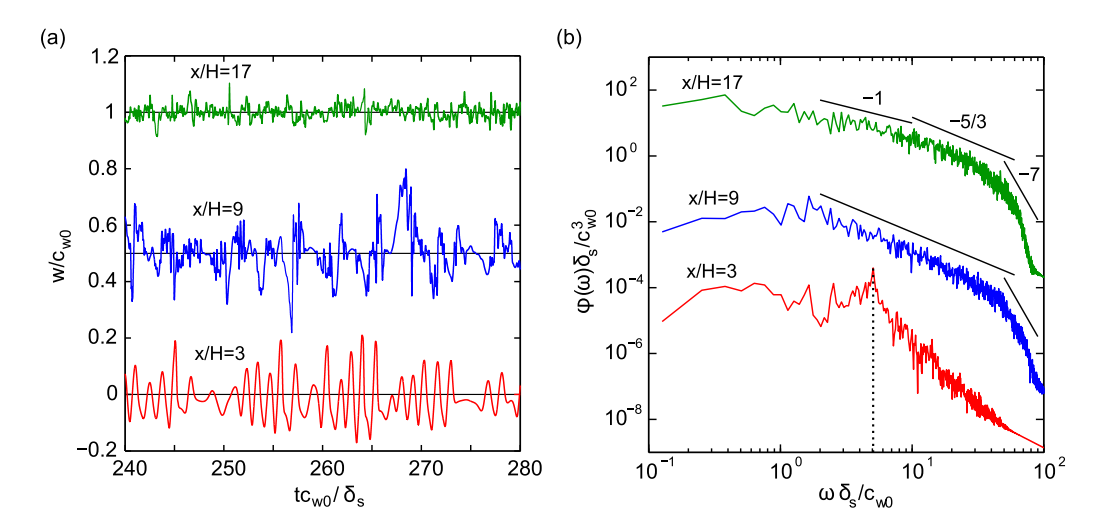


FIG. 9. (a) Typical time series of wall-normal velocity w sampled at x = 3H ($\approx 1.3\lambda_w$), x = 9H ($\approx 3.9\lambda_w$), and x = 17H ($\approx 7.3\lambda_w$), all at z = 0.025H($\approx 0.183\delta_s$) at the midspan. The signals are equally separated vertically by one half unit. (b) Single-point frequency spectra of turbulent kinetic energy for fluctuation signals sampled at the same locations presented in (a). The spectrum for x = 9H is shifted by twofold upward, the spectrum for x = 17H is shifted by fourfold upward, all relative to one for x = 3H. Reference lines with slopes of -1, -5/3, and -7 are included. Vertical dashed line indicates the vortex shedding frequency.

The maximum vertical velocity associated with the shed vortices of an ISW propagating in the absence of background current has been measured within the range of $0.02 < w/c_{w0} < 0.06$ in the laboratory measurement conducted by Carr *et al.* [11] and $0.1 < w/c_{w0} < 0.7$ in the two-dimensional numerical simulation conducted by Aghsaee *et al.* [7]. According to Aghsaee *et al.*, such a difference is attributed to the Reynolds number effect. The Reynolds number resides in the range $0.6 \times 10^5 < \text{Re}_w < 0.65 \times 10^5$ for the former case and in $1.8 \times 10^5 < \text{Re}_w < 5.8 \times 10^5$ for the latter case. The present study ($\text{Re}_w = 1.6 \times 10^5$), with a finite background current and demonstrated three-dimensionality and turbulence, cannot be directly compared to these previous investigations. Restricting one's perspective to Reynolds number, however, the vertical velocity in the present case compares relatively well with the numerical results of Aghsaee *et al.* to the leading order, at least in the earlier stages of wave-induced BBL development. The large vertical velocity reported by Aghsaee *et al.* might be attributed to a two-dimensional artifact in addition to the Reynolds number effect. Compared to their two-dimensional counterparts, three-dimensional vortices are effectively less coherent in the transverse, with the degree of coherence further impacted with increasing Reynolds number.

Figure 9(b) shows frequency spectra of turbulent kinetic energy processed from the field signals at the same locations discussed above. Spectra are calculated by adopting the same methodology used by Jones *et al.* [51]. The signals are sampled at every time step, and the sampling interval is of $3.27\lambda_w/c$, which corresponds to approximately 90 vortex shedding cycles. At the tail of the separation bubble (x = 3H) the vortex shedding frequency of $\omega = 5.07c_{w0}/\delta_s$ is dominant. In the burst stage (x = 9H) higher frequency components gain much more energy due to the down-scale cascade, and the largest energy is attained at the frequency $\omega = 1.65c_{w0}/\delta_s$ that is much lower than the fundamental shedding frequency. This up-scale energy cascade is a manifestation of pairing and merger of the shed vortices that still operate embedded in a turbulent flow background. At the developing turbulent boundary layer stage (x = 17H), such a low-frequency energy is substantially diminished.

In the same figure, reference lines with slopes of -1, -5/3, and -7 are also included. A wide frequency range of -5/3 spectral slope is visible in the turbulent-cloud formation stage. In the

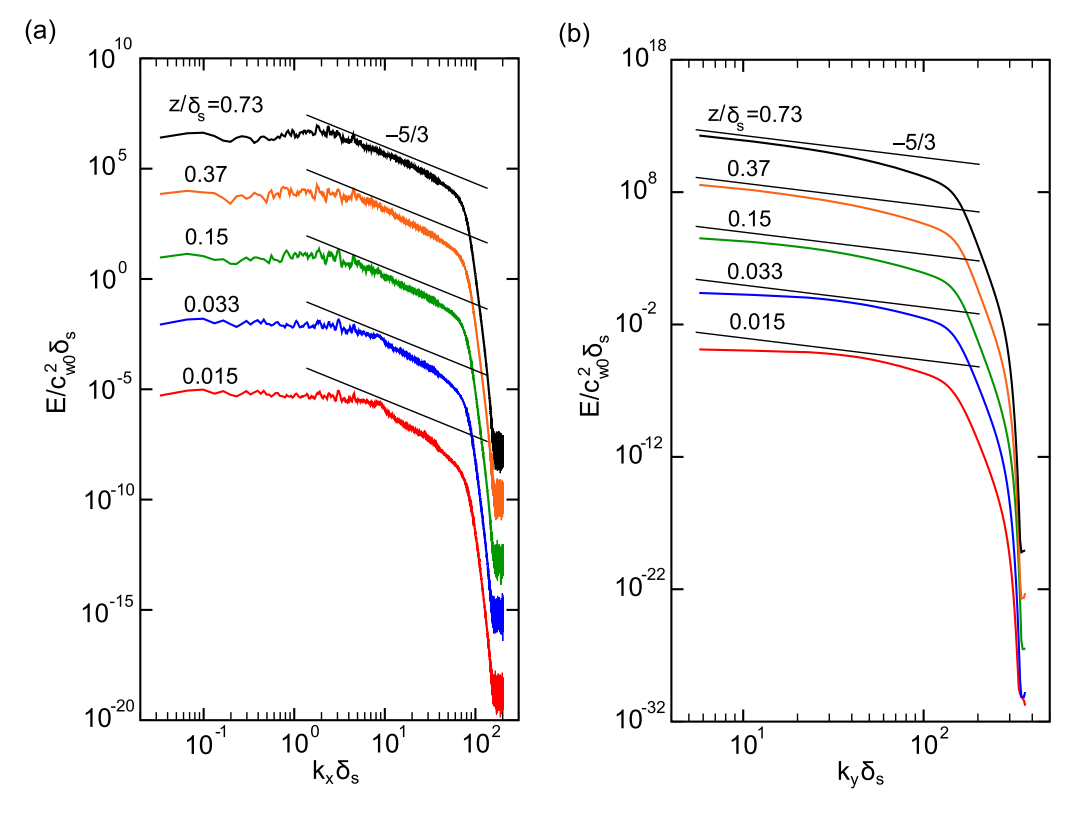


FIG. 10. Time-averaged one-dimensional turbulent kinetic energy spectra at $z/\delta_s = \{0.015, 0.033, 0.15, 0.37, 0.73\}$ together with -5/3 slope. (a) Streamwise spectra. All cases are separated by threefold in vertical direction starting from the case $z/\delta_s = 0.015$. (b) Spanwise spectra. All cases are separated by 2.5-fold starting from the case $z/\delta_s = 0.015$.

developing turbulent boundary layer stage, a -1 slope spectrum emerges at low frequencies. These spectral slopes (-1, -5/3, and -7) are also observed by Wu and Moin [52] in their DNS simulation of a zero-pressure-gradient flat-plate boundary layer flow. The -1 slope is also reported by Turan *et al.* [53] for a flat-plate turbulent boundary layer and by Perry *et al.* [54] for a turbulent pipe flow.

A complementary perspective in terms of relevant spatial scales is also gained by examining one-dimensional turbulent kinetic energy spectra in the streamwise and spanwise direction. Figure 10(a) shows such time-averaged, one-dimensional, streamwise-computed energy spectra obtained at several different wall-normal offsets in the range $0.015 \le z/\delta_s \le 0.73$. These spectra are computed over the full streamwise extent of the computational domain. Following a flat spectrum at the lowest wave numbers, the intermediate wave numbers have a steeper spectral slope, which becomes larger than -5/3, as it approaches the bottom boundary; a -5/3 spectrum is recovered away from the boundary, at $z = 0.73\delta_s$. Such a faster rate of spectral energy decay near the wall has an important implication to the wake relaxation in the viscous-wall region, as will be discussed in detail in Part II of this study. Although the streamwise spectra drop off by four to five orders of magnitude across wave numbers not directly impacted by the spectral filter, they are less smooth when compared to the transverse spectra discussed below. In particular, a small band of very low-amplitude noise is visible near the highest resolved wave numbers. This noise can be reduced by sampling across more statistically independent snapshots of the flow, a task necessitating nontrivial computational cost in the form of additional time integration of the governing equations. Given the spectral drop-off of

over 10-fold across all resolved scales; nevertheless, this high-wave-number noise is negligible for practical purposes.

In Fig. 10(b) the corresponding energy spectra in the transverse direction are shown. Contrary to their streamwise counterpart, the spectral curves have a much smoother structure across the entire range of wave numbers. There is a slight indication of a -5/3 range near the lowest wave number for the case of $z = 0.73\delta_s$. The lack of the inertial range in the transverse energy spectrum is not uncommon in numerical simulations of turbulent flows, such as DNS simulations of turbulent boundary layer by Spalart [55] and of self-similar mixing layer by Rogers and Moser [56], in which insufficient Reynolds number (Spalart) and insufficient spanwise domain size (Rogers and Moser) are typically suggested as the potential causes. Nevertheless, the domain width of the present study is sufficient with respect to its objectives. On one hand, it has been confirmed that the transverse correlation drops down to negative in the turbulent boundary layer (not shown). Moreover, the present domain width is sufficiently large to resolve the self-excited instabilities which lead to a self-sustained turbulent flow.

V. CONCLUDING REMARKS

The separated boundary layer flow in the footprint of a large-amplitude ISW of depression propagating against an oncoming barotropic current is investigated numerically using high-resolution implicit LES. To the authors' best knowledge, this is the first systematic three-dimensional investigation of the self-sustained generation of episodic vortex shedding, the resulting transition and ultimate formation of a turbulent BBL under an ISW. The present work (Part I) mainly focuses on the three-dimensional flow structure of all the above stages in BBL development.

The vortex shedding is intrinsically excited by an asymptotically two-dimensional instability of the nearly parallel separated shear layer in the long separation bubble formed at the downstream side of the wave footprint. This two-dimensional, linear global oscillator is *self-excited* by a three-dimensional, stationary global mode possessing a transverse coherent structure along the shear layer and bottom boundary; such a three-dimensional instability is evidently not accessible in 2D simulations.

Each excited transverse instability wave at the shear layer is periodically shed, together with a vortex, from the tail of the separation bubble; the wave remains inside of the vortex core. Such an axial disturbance, which is manifested as a layer of streamwise vorticity in the shed vortex, subsequently excites an elliptic instability mode, bending the vortex core.

As the shed vortices pair, merge, and roll over the bottom boundary downstream, the layer of streamwise vorticity is stretched circumferentially, virtually forming a roll of the vorticity layer inside of the vortex. (Note here that the vorticity layer stretching does not refer to an axial stretching of the vortex core; descriptively, it is more like a stretching of a material surface.) The associated vorticity layer at the bottom boundary also stretches and wraps around the vortex. Such a roll of stretched circumferential vorticity sheets starts to degenerate through formation of coherent, streamwise vortex streaks excited by a short-wave instability, and the primary vortex is populated by such coherent vortices. The primary vortex then rapidly and entirely breaks up through strong nonlinear processes from interior to exterior, forming a "cloud" of small eddies. The turbulent cloud further expands downstream. Through these physical processes, the wave-induced near-bed turbulence is both self-excited and *self-sustained*: No external perturbations are needed to trigger the vortex shedding and to continually drive the turbulent BBL under the propagating ISW.

The vigorous vortex shedding is a characteristic signature of the ISW-impressed adverse pressure gradient exerting over the bed beneath the aft half of the wave. Following the turbulent cloud formation stage, around 15 water column depths downstream of the wave, this discrete signature becomes obscured and nearly lost, such that the agglomerated turbulent clouds lose their alternating pattern of local updraft and downdraft; and the turbulent wake is relaxed to a flat-plate turbulent

boundary layer (Fig. 8). Such a relaxation process is similar to the case of a shorter separation bubble encountered in an aerodynamic separating flow [40]. This will be detailed by analyses of flow statistics given in the companion paper of this study (Part II). As will be shown in Part II, the Blasius boundary layer profile at the oncoming flow is also completely "forgotten" and altered to that of a zero-pressure-gradient turbulent boundary layer in the regime (iii), in which the Blasius boundary layer may appear not primarily important in sustaining the turbulence. Nonetheless, the near-bed vertical shear of the background current U'(z), not limited to the Blasius boundary layer in general, implicitly and continually supplies kinetic energy to the turbulence through the production term $(-u'w'\partial \overline{u}/\partial z)$, which is expected to contribute to sustain the turbulent boundary layer far downstream of the wave. Future investigation is needed, to verify such a role of near-bed vertical shear of the background current.

A fundamental difference of the experimental studies conducted by Carr and Davies [9] and Aghsaee and Boegman [12] with the work reported here is that no background current is, at least intentionally, introduced. As reported in our previous work [19], a two- or three-dimensional numerical simulation with no background current with sufficient resolution of the relevant near-bed scales cannot generate spontaneously any vortex shedding; specific volumetric forcing needs to be introduced [51] and is kept active at all times. Such an observation is consistent with the analysis of Vershaeve and Pedersen [13] who found that the BBL under an ISW propagating into quiescent water is convectively unstable: Any instantaneously inserted disturbances into the BBL will produce a transient instability, with any vortical structures advected downstream of the wave trough; the BBL then relaminarizes.

Because of the highly expensive computational cost, the present study focuses on one representative case in a nontrivial parameter space which consists of the wave-based Reynolds number, or variants thereof, the ISW amplitude, the structure and strength of the stratification profile and strength (which directly impacts wave polarity) and the associated BBL structure of background current. The physical properties of the near-bed wake examined here are found to be largely dependent on the mean flow structure, itself intimately connected to the background current strength. As such, the corresponding physical properties would be considerably different for flow configurations residing in radically different parts of the above parameter space. In the longer term, a characterization of the wave-induced turbulence under such different and oceanically representative environmental base-states is imperative and is expected to provide useful insights in modeling the wave drag and wave-induced sediment resuspension. Such a characterization, inevitably involving a broad sweep of parameter space, would be enabled by the availability of more powerful computing resources together with reduced resolution LES. The reduced resolution LES would critically need to be coupled to an optimally chosen subgrid scale turbulence model whose fidelity has been demonstrated for separating flows, much like the study of Cadieux et al. [41] conducted for a canonical separation bubble.

ACKNOWLEDGMENTS

The support of Office of Naval Research Grant No. N00014-11-1-0511 and National Science Foundation OCE CAREER Grant No. 0845558 are gratefully acknowledged. P.J.D. acknowledges additional support by National Science Foundation OCE Grant No. 1634257. The authors thank Prof. L. G. Redekopp for numerous inspiring conversations on this problem. We thank Dr. P. Meunier for insightful advice regarding the elliptic instability. Additional insightful discussions with Prof. J. A. Domaradzki and Dr. F. Cadieux are also acknowledged. High-performance computing resources were provided through the US Department of Defense High Performance Computing Open Resource Systems. We thank two anonymous referees for their constructive comments that significantly improved the initial manuscript. P.J.D. thanks in particular Prof. Marek Stastna, Prof. Magda Carr, Prof. Kevin Lamb, Prof. Peter Davies, Prof. Leon Boegman and Prof. Ben Reeder and Dr. Ren-Chieh Lien and Dr. Payam Aghsaee for a number of illuminating discussions over the years.

- [1] D. Bogucki, T. Dickey, and L. G. Redekopp, Sediment resuspension and mixing by resonantly generated internal solitary waves, J. Phys. Oceanogr. 27, 1181 (1997).
- [2] D. Bogucki and L. G. Redekopp, A mechanism for sediment resuspension by internal solitary waves, Geophys. Res. Lett. **26**, 1317 (1999).
- [3] B. Wang and L. G. Redekopp, Long internal waves in shear flows: Topographic resonance and wave-induced global instability, Dyn. Atmos. Oceans 33, 263 (2001).
- [4] M. Stastna and K. G. Lamb, Vortex shedding and sediment resuspension associated with the interaction of an internal solitary wave and the bottom boundary layer, Geopys. Res. Lett. 29, 1512 (2002).
- [5] M. Stastna and K. G. Lamb, Sediment resuspension mechanism associated with internal waves in coastal oceans, J. Geophys. Res. 113, C10016 (2008).
- [6] P. J. Diamessis and L. G. Redekopp, Numerical investigation of solitary intenal wave-induced global instability in shallow water benthic boundary layers, J. Phys. Oceanogr. 36, 784 (2006).
- [7] P. Aghsaee, L. Boegman, P. J. Diamessis, and K. Lamb, Boundary-layer-separation-driven vortex shedding beneath internal solitary waves of depression, J. Fluid Mech. 690, 321 (2012).
- [8] M. Carr and P. A. Davies, The motion of an internal solitary waves of depression over a fixed bottom boundary in a shallow, two-layer fluid, Phys. Fluids 18, 016601 (2006).
- [9] M. Carr and P. A. Davies, Boundary layer flow beneath an internal solitary wave of elevation, Phys. Fluids **22**, 026601 (2010).
- [10] Ø. Theim, M. Carr, J. Berntsen, and P. A. Davies, Numerical simulation of internal solitary wave-induced reverse flow and associated vortices in a shallow, two-layer fluid benthic boundary layer, Ocean Dynam. 61, 857 (2011).
- [11] M. Carr, P. A. Davies, and P. Shivaram, Experimental evidence of internal solitary wave-induced global instability in shallow water banthic boundary layers, Phys. Fluids **20**, 066603 (2008).
- [12] P. Aghsaee and L. Boegman, Experimental investigation of sediment resuspension beneath internal solitary waves of depression, J. Geophys. Res. Oceans 120, 3301 (2015).
- [13] J. C. G. Vershaeve and G. K. Pedersen, Linear stability of boundary layers under solitary waves, J. Fluid Mech. 761, 62 (2014).
- [14] J. Olsthoorn, M. Stastna, and N. Soontiens, Fluid circulation and seepage in lake sediment due to propagating and trapped internal waves, Water Resour. Res. 48, W11520 (2012).
- [15] S. Harnanan, N. Soontiens, and M. Stastna, Internal wave boundary layer interaction: A novel instability over broad topography, Phys. Fluids 27, 016605 (2015).
- [16] S. Harnanan, M. Stastna, and N. Soontiens, The effects of near-bottom stratification on internal wave induced instabilities in the boundary layer, Phys. Fluids **29**, 016602 (2017).
- [17] C. Xu, C. Subich, and M. Stastna, Numerical simulations of shoaling internal solitary waves of elevation, Phys. Fluids 28, 076601 (2016).
- [18] L. Boegman and M. Statsna, Sediment resuspension and transport by internal waves, Annu. Rev. Fluid Mech. 51, 129 (2018).
- [19] T. Sakai, P. D. Diamessis, and G. B. Jacobs, Large eddy simulations of turbulence under internal solitary wave of depression, in *Proceedings of the VIIIth International Symposium on Stratified Flows* (University Corporation for Atmospheric Research, Boulder, 2016).
- [20] M. Stastna and K. G. Lamb, Large fully nonlinear internal solitary waves: The effect of background current, Phys. Fluids 14, 2987 (2002).
- [21] M. Dunphy, C. Subich, and M. Stastna, Spectral methods for internal waves: Indistinguishable density profiles and double-humped solitary waves, Nonlin. Proc. Geophys. 18, 351 (2011).
- [22] B. Turkington, A. Eydeland, and S. Wang, A computational method for solitary intenal waves in a continuously stratified fluid, Stud. Appl. Math. 85, 93 (1991).
- [23] L. Lamb and B. Wan, Conjugate flows and flat solitary waves for a continuously stratfied fluid, Phys. Fluids 10, 2061 (1998).
- [24] D. Fructus, M. Carr, J. Grue, A. Jansen, and P. Davies, Shear-induced breaking of large internal solitary waves, J. Fluid Mech. **620**, 1 (2009).
- [25] M. F. Barad and O. B. Fringer, Simulations of shear instabilities in interfacial gravity waves, J. Fluid Mech. 644, 61 (2010).

- [26] K. G. Lamb and D. Farmer, Instabilities in an internal solitary-like wave on the Oregon Shelf, J. Phys. Oceanogr. 41, 67 (2011).
- [27] C. Xu, M. Stastna, and D. Deepwell, Spontaneous instability in internal solitary-like waves, Phys. Rev. Fluids 4, 014805 (2019).
- [28] K. G. Lamb, Shoaling internal solitary waves: On a criterion for the formation of waves with trapped cores, J. Fluid Mech. **478**, 81 (2003).
- [29] R.-C. Lien, E. A. D'Asaro, F. Henyey, M.-H. Chang, T.-Y. Tang, and Y.-J. Yang, Trapped core formation within a shoaling nonlinear internal wave, J. Phys. Oceanogr. 42, 511 (2012).
- [30] Y. He, K. G. Lamb, and R.-C. Lien, Internal solitary waves with subsurface cores, J. Fluid Mech. 873, 1 (2019).
- [31] G. Rivera-Rosario, P. J. Diamessis, R.-C. Lien, K. G. Lamb, and G. N. Thomsen, Formation of recirculating cores in convectively breaking internal solitary waves of depression shoaling over gentle slopes in the South China Sea, J. Phys. Oceanogr. 50, 1137 (2020).
- [32] R.-C. Lien, F. Henyey, B. Ma, and Y.-J. Yang, Large-amplitude internal solitary waves observed in the Northern South China Sea: Properties and energetics, J. Phys. Oceanogr. 44, 1095 (2014).
- [33] Z. Shuang, M. H. Alford, and J. B. Mickett, Characteristics, generation and mass transport of nonlinear internal waves on the Washington continental shelf, J. Geophys. Res. Oceans 120, 741 (2015).
- [34] D. Rodríguez, E. M. Gennaro, and M. P. Juniper, The two classes of primary modal instability in laminar separation bubbles, J. Fluid Mech. 734, R4-1 (2013).
- [35] D. Rodríguez and E. M. Gennaro, On the secondary instability fo forced and unforced laminar sepration bubbles, Proc. IUTAM 14, 78 (2015).
- [36] T. Cebeci, Stability and Transition: Theory and Application (Springer, Berlin, 2004).
- [37] A. P. Zulberti, G. N. Ivey, and N. L. Jones, Observations of near-bed stress beneath nonlinear internal wave trains in the ocean, in *Proceedings of the 21st Austrarian Fluid Mechanics Conference* (Australasian Fluid Mechanics Society, Perth, 2018).
- [38] P. J. Diamessis, J. A. Domaradzki, and J. S. Hesthaven, A spectral multidomain penalty method model for the simulation of high Reynolds number localized stratified turbulence, J. Comput. Phys. 202, 298 (2005).
- [39] P. R. Spalart and M. K. Strelets, Mechanisms of transition and heat transfer in a separation bubble, J. Fluid Mech. 403, 329 (2000).
- [40] M. Alam and N. D. Sandham, Direct numerical simulation for 'short' laminar separation bubbles with turbulent reattachment, J. Fluid Mech. 403, 223 (2000).
- [41] F. Cadieux, J. A. Domaradzki, T. Sayadi, S. Bose, and F. Duchaine, DNS and LES of separated flows at moderate Reynolds numbers, J. Fluids Eng. 136, 060902 (2014).
- [42] P. G. Drazin and W. H. Reid, Hydrodynamic Stability (Cambridge University Press, Cambridge, UK, 2004).
- [43] V. Theofilis, Global linear instability, Annu. Rev. Fluid Mech. 43, 319 (2011).
- [44] D. Rodríguez and V. Theofilis, Structural changes of laminar separation bubbles induced by global linear instability, J. Fluid Mech. 655, 280 (2010).
- [45] R. R. Kerswell, Elliptic instability, Annu. Rev. Fluid Mech. 34, 83 (2002).
- [46] F. Waleffe, On the three-dimensional instability of strained vortices, Phys. Fluids A 2, 76 (1990).
- [47] P. Meunier and T. Leweke, Elliptic instability of a co-rotating vortex pair, J. Fluid Mech. 533, 125 (2005).
- [48] T. Leweke and C. H. K. Williamson, Cooperative elliptic instability of a vortex pair, J. Fluid Mech. 360, 85 (1998).
- [49] P. J. Diamessis and K. K. Nomura, Interaction of vorticity, rate-of-strain and scalar gradient in stratified homogeneous sheared turbulence, Phys. Fluids 12, 1166 (2000).
- [50] J. Jeong and F. Hussain, On the identation of a vortex, J. Fluid Mech. 285, 69 (1995).
- [51] L. E. Jones, R. D. Sandberg, and N. D. Sandham, Direct numerical simulations of forced and unforced separation bubbles on an airfoil at incidence, J. Fluid Mech. 602, 175 (2008).
- [52] X. Wu and P. Moin, Direct numerical simulation of turbulence in a nominally zero-pressure-gradient flat-plate boundary layer, J. Fluid Mech. 630, 5 (2009).
- [53] O. Turan, R. S. Azad, and S. Z. Kazzab, Experimental and theoretical evaluation of k_1^{-1} spectral law, Phys. Fluids **30**, 3463 (1987).

SAKAI, DIAMESSIS, AND JACOBS

- [54] A. E. Perry, S. Henbest, and M. S. Chong, A theoretical and experimental study of wall turbulence, J. Fluid Mech. **165**, 163 (1986).
- [55] F. R. Spalart, Direct simulation of a turbulent bounday layer up to $R_{\theta} = 1410$, J. Fluid Mech. 187, 61 (1988).
- [56] M. M. Rogers and R. D. Moser, Direct simulation of a self-similar turbulent mixing layer, Phys. Fluids 6, 903 (1994).